Journal of Catalysis 401 (2021) 262–270

Contents lists available at ScienceDirect

Journal of Catalysis

journal homepage: www.elsevier.com/locate/jcat

Construction of p-n junctions in single-unit-cell $ZnIn_2S_4$ nanosheet arrays toward promoted photoelectrochemical performance

Yu Wu [a], Shukai Yao [c], Guangzhen Lv [a], Yanwei Wang [a], Huijuan Zhang [a], Peilin Liao [c], Yu Wang [a,b]

[a] The School of Chemistry and Chemical Engineering, State Key Laboratory of Power Transmission Equipment & System Security and New Technology, Chongqing University, 174 Shazheng Street, Shapingba District, Chongqing City 400044, PR China
[b] The School of Electrical Engineering, Chongqing University, 174 Shazheng Street, Shapingba District, Chongqing City 400044, PR China
[c] The School of Materials Engineering, Purdue University, West Lafayette, IN 47906, USA

ARTICLE INFO

Article history:
Received 5 May 2021
Revised 14 July 2021
Accepted 1 August 2021
Available online 8 August 2021

Keywords:
Phosphorus incorporation
Single-unit-cell $ZnIn_2S_4$
P-n junctions
Carrier separation/transport
Photoelectrochemical water splitting

ABSTRACT

The realization of semiconductor p–n junctions is essential for improved photoelectrochemical (PEC) performance in water splitting. Concerning the traditional p-n junctions, although the p- and n-type materials that are utilized to build them have been decreased from bulk to only two unit cells, the PEC water splitting efficiency is still tough to be satisfactory due to the obstacle of interlayer carrier separation/-transport. Herein, we report that p-n junctions based on n-type (sulfur vacancies) and p-type (phosphorus incorporation) domains of single-unit-cell thick $ZnIn_2S_4$ (ZIS) nanosheet arrays present a quite different carrier separation/transport characteristic. As a result, such peculiar nanostructure of the optimal phosphorus-incorporated n-type ZIS (n-ZIS-P) photoelectrode delivers the highest photogenerated current density of 6.34 mA cm^{-2} at 1.23 V versus reversible hydrogen electrode (V_{RHE}) among all the reported ZIS-based photoanodes. Besides, the hydrogen and oxygen production in the stoichiometric ratio (2:1) is achieved at a Faradaic efficiency of almost unity.

1. Introduction

Solar-driven photoelectrochemical (PEC) water splitting to hydrogen fuel has been an ideal avenue for clean energy storage and conversion [1–4]. So far, a great variety of semiconductor materials have been researched and applied to PEC devices, however, most of the photocatalysts are still subjected to limited photoactivity as a result of the high recombination rate of photoexcited charges [5,6]. Tailoring ultrathin morphology [7,8] and building *p-n* junctions [9–12] have been proven capable of optimizing the PEC performance. For some *n*-type materials (such as metal oxides, chalcogenides, and g-C_3N_4), there have been wide studies on the construction of *p-n* junctions via group V elements acceptor-doping [13–15]. In terms of the traditional *p-n* junctions, the materials employed for constructing such structures have attained their theoretical limit of the thickness (two unit cells thick). For example, Philip Kim and co-workers proposed the ultrathin *p-n* heterojunctions formed by van der Waals interactions [16]. However, the obstacle in interlayer carrier separation and transport is common for such structures. Consequently, we concentrate on the sheet-like nanomaterials based on thinner limit thickness (merely one unit-cell thickness) for creating *p–n* junctions to tackle the above problems.

Here, we first construct *p-n* junctions through phosphine (PH_3) treatment of single-unit-cell *n*-type $ZnIn_2S_4$ (*n*-ZIS) layer arrays exhibiting completely diverse carrier separation and transportation behaviors. Consequently, such peculiar nanostructure endows the optimal phosphorus-incorporated *n*-ZIS (*n*-ZIS-P) photoanode with a high oxygen evolution rate of 51.5 μmol $cm^{-2}h^{-1}$ and an impressive photogenerated current density of 6.34 mA cm^{-2} at 1.23 V versus the reversible hydrogen electrode (V_{RHE}), much better than those of *n*-ZIS. Of note, the best value of photocurrent density we display in this work is higher than all the ZIS-based photoanodes. The significant improvement may be mainly due to the facilitated charge separation/transport, prohibited electron-hole recombination, prolonged charge lifetime, and improved photostability.

2. Experimental

2.1. Synthesis of n-ZIS nanostructures

In the synthetic process, 0.6 mmol $ZnCl_2$, 1.2 mmol $InCl_3{\cdot}4H2O$, 2.4 mmol CH_4N_2S, and 60 mL deionized water were mixed by constant magnetic stirring for 20 min. Subsequently, 10 μL $(NH_4)_2S$

E-mail addresses: lpl@purdue.edu (P. Liao), wangy@cqu.edu.cn (Y. Wang)

https://doi.org/10.1016/j.jcat.2021.08.009
0021-9517/

was added drop by drop in the above solution with constant magnetic stirring for 10 min. Afterward, 5 mL of the reaction solution and the plasma-cleaned Fluorine-doped tin oxide glass (FTO) substrates were placed in Teflon-lined stainless steel autoclaves. After heating at 160 °C for 6 h, they were naturally cooled down to room temperature, yellow two-dimensional *n*-ZIS nanosheet arrays were formed on FTO substrates, which were rinsed thoroughly with deionized water and ethanol repeatedly, and dried in a vacuum oven at a temperature of 50 °C.

2.2. Fabrication of n-ZIS-P nanostructures

The *n*-ZIS electrodes were placed in a tube furnace, and then were rapidly heated to 400 °C in argon (Ar) atmosphere. When the temperature reached 400 °C, PH_3 flow started to fill the system, and both the time for filling with PH_3 and the dwell time were controlled for 1 min. The flow rate ratios of $PH_3/(PH_3 + Ar)$ were 1%, 3%, 5%, 7%, and 9%, while the total flow rate of Ar and PH_3 was kept at 100 mL·min^{-1}. After naturally cooling down to room temperature, the *n*-ZIS-P photoanodes were carefully taken out for further measurements.

2.3. Photodeposition experiments

20 μM H_2PtCl_6, 20 μM $AgNO_3$, 0.4 mM $MnCl_2$, and 0.4 mM $CoSO_4$ were used as metal precursors for Pt, Ag, MnOx, and CoO_x photodeposition, respectively. The samples with FTO were immersed in 50 mL aqueous solution mixed with a metal precursor. The systems were evacuated for 30 min to completely remove the dissolved air. Then, the photodeposition reactions were carried out upon AM 1.5G illumination for 5 min and the intensity was 100 mW cm^{-2}. After irradiation, the samples were washed with deionized water and ethanol thoroughly, and were subsequently dried in a vacuum oven overnight.

2.4. Physical and chemical characterization

The scanning electron microscopy (SEM) images of the samples was conducted using a JEOL-7800F field emission SEM. X-ray diffraction (XRD) patterns were recorded on a PANalytical X'Pert Powder X-ray diffractometer with Cu Kα radiation. The microstructure of the products were characterized via a FEI Talos F200X transmission electron microscopy (TEM) with an energy-dispersive X-ray spectroscopy (EDS) detector and high-resolution TEM (HRTEM). Elemental mappings of EDS were performed on the high-angle annular dark field – scanning TEM (HAADF-STEM). Atomic force microscopy (AFM) was conducted by using MFP-3D-BIO to identify the thickness. An ESCALAB 250Xi X-ray photoelectron spectrometer (XPS) from Thermo Fisher Scientific was undertaken to investigate the element valence status of the samples, with monochromatic Al Kα radiation (225 W, 15 mA, 15 kV). The Raman spectra of the as-prepared products were studied by LabRAM HR Evolution spectrometer. A UV-3600 spectrophotometer equipped with an integrating sphere (SHIMADU, Japan) was used to record the ultraviolet–visible diffused reflectance spectra (UV–vis DRS). An iCAP 6300 Duo inductively coupled plasma optical emission spectrometer (ICP-OES) was used to determine the elemental information. Ultraviolet photoemission spectroscopy (UPS) measurements were carried out on a spectrometer (ESCA LAB 250 Xi) with He I Source Gun of 21.22 eV. A FLS1000 spectrofluorometer equipped with both continuous (450 W) and pulsed xenon lamps were conducted to collect the steady-state photoluminescence (PL) spectra (excited by 330 nm illumination) and the time-resolution PL (TRPL) spectra. Surface photovoltaic (SPV) properties of products were measured using a surface photovoltage test system (CEL-SPS1000).

2.5. Photoelectrochemical measurements

The photoelectrochemical (PEC) performance of the photoanodes was investigated by means of a controllable reaction system (CEL-PAEM-D8, CEAULight, China) with 150 mL volume. The light source was a commercial solar simulator (100 mW cm^{-2}, CEL-HXF300, CEAULight, China) equipped with an air mass filter (AM 1.5G). A CHI 760E electrochemical workstation was conducted to probe PEC performance in 0.5 M Na_2SO_4 or 0.5 M Na_2SO_3 aqueous solution using a three-electrode configuration (the as-prepared sample served as a working electrode; platinum wire served as counter electrode; saturated Ag/AgCl electrode served as a reference electrode). The scan rate of 10 mV s^{-1} was undertaken to test the photocurrent density–voltage (*J-V*) and photocurrent density-time (*J-t*) curves under irradiation. Electrochemical impedance spectra (EIS) (0.1 Hz to 100 kHz) were recorded in the three-electrode system in the darkness/irradiation. The frequency of 1.0 kHz was conducted to record Mott-Schottky (M−S) plots with the amplitude of 10 mV without illumination. All the obtained potentials versus reversible hydrogen electrode (RHE) were determined based on the Nernst equation: $E_{RHE} = E_{Ag/AgCl} + 0.059pH + 0.1976$ V. The photocurrent density is decided by the formula as $J_{PEC} = J_{abs} \times \eta_{separation} \times \eta_{injection}$, where J_{PEC} corresponds to the experimentally obtained photocurrent density, J_{abs} represents the J_{PEC} assuming the internal quantum efficiency of 100%, $\eta_{separation}$ represents the separation efficiency of carriers, and $\eta_{injection}$ refers to the injection efficiency of carriers, respectively. Due to the oxidation thermodynamics and kinetics of hole scavengers (e.g. Na_2SO_3) are facile enough, the $\eta_{injection}$ could be almost assumed to be 100% with the presence of Na_2SO_3. Therefore, $\eta_{separation}$ can be calculated by dividing J_{PEC} (in Na_2SO_3) by J_{abs} [17–19]. The half-cell solar-to-hydrogen energy efficiency (HC-STH) of as-prepared photoanodes were calculated by the results of *J-V* curves, and based on the formula: HC-STH (%) = $J \times (1.23 - V_{RHE}) \times 100\%$, in which J (mA cm^{-2}), V stands for the electrode potential versus RHE. The monochromatic irradiation from a Xe lamp equipped with optical filters was utilized to record incident photon to current efficiency (IPCE). The IPCE at each wavelength was determined from the equation: IPCE = $(1240\,J)/(\lambda I_{light}) \times 100\%$, where J corresponds to the photocurrent density (mA cm^{-2}) at a selected wavelength, λ is the wavelength (nm) of the incident light, and I_{light} refers to the irradiance intensity (mW cm^{-2}). The yield of oxygen and hydrogen were measured using a gas chromatograph (Aulight GC-7920).

2.6. Theoretical calculation

We have used VASP version 5.4.4 to conduct the first-principles density functional theory (DFT) calculations [20,21]. The projector augmented wave (PAW) method [22] was used, and the 3*s*3*p* orbitals of P, 3*s*3*p* orbitals of S, 3*d*4*s* orbitals of Zn and 4*d*5*s*5*p* orbitals of In are treated as valence electron orbitals. The Perdew-Burke-Ernzerhof (PBE) [23] exchange correlation functional was chosen. The Hubbard corrected DFT (DFT + U) method [24,25] was applied with the Hubbard U for Zn 3*d* and In 4*d* set at 4.5 and 4.8 eV, respectively, to correct for the self-interaction among localized *d* electrons. The U value for Zn was set according to the previously tested value for Zn in ZnO [26], and the U value for In was set to be the same as that for Sn in Cu_2ZnSnS_4 [27] because of their similar closed shell electronic configurations. The optimized bulk $ZnIn_2S_4$ crystal has lattice constants of $a = b = 3.884$ Å and $c = 12.512$ Å, in close agreement with the experimental lattice constants of $a = b = 3.850$ Å and $c = 12.340$ Å [28]. A (4×4) (0001) $ZnIn_2S_4$ slab model of seven atomic layers thick was built from the optimized crystal structure, which consists of 112 atoms along with a vacuum layer 15 Å thick. For structures with defects, S vacancies

were introduced by removing two S atoms from the top layer. P dopants were introduced by replacing two S atoms at the bottom layer by P atoms. To keep the two defects apart from each other, the vacancies or dopants were positioned at the corner and the center of the atomic layer, respectively. These S vacancies at the top and P dopants at the bottom configuration were found to be 4.55 eV lower in total energy compared to the opposite arrangement with S vacancies at the bottom and P dopants at the top. Atomic positions were fully relaxed with a $2 \times 2 \times 1$ k-point mesh and a 400 eV kinetic energy cut-off. Gaussian smearing was chosen with a smearing parameter of 0.1 eV. Self-consistent electronic steps converge when the total energy difference between two steps is less than 1×10^{-5} eV. The force convergence criterion was 0.025 eV/Å on each atom. For electronic structure calculations, a denser k-point grid of $4 \times 4 \times 1$ was implemented, and the tetrahedral smearing method was used. The charge density difference was calculated by subtracting the total density of pure ZIS from the doped structure and ensuring a proper atomic balance by adding or subtracting S or P atoms. For example, the density difference for the ZIS in the P doping case was calculated by $\rho_{P:ZIS} - \rho_{pure\ ZIS} - \rho_{P} + \rho_{S}$. The value of isosurface is 0.0015 e/Bohr^3.

3. Results and discussion

3.1. Investigation of the roles of sulfur vacancies and phosphorus incorporation by DFT calculations

Firstly, the roles of sulfur (S) vacancies and phosphorus (P) atoms incorporation in the electronic configuration for ZIS were probed using DFT computations. And the selection of model structure is based on defect formation energy (Table S1). According to the results of Table S1, the introduction of P doping at the bottom (the In facet) would make the configuration with sulfur vacancies more stable, indicating that the P atoms tend to be incorporated at the bottom (the In facet). The calculated projected density of states (PDOS) for pure ZIS, ZIS with S vacancies, and ZIS with P incorporation were shown in Fig. 1a-c, respectively. For the PDOS of pure ZIS (Fig. 1a), peaks near the valance band maximum (VBM) consist of hybridized S *3p* and Zn *3d* states, while at ~1.8 eV below VBM, large peaks of S *3p* states appear, in agreement with previous computational work [29]. In comparison to the pure ZIS, the Fermi level (E_F) for ZIS with S vacancies shifted upwards into the unoccupied states near the conduction band minimum (CBM), showing *n*-type character [30,31]. By contrast, the E_F of P-incorporated ZIS moved downwards and was close to VBM, bringing acceptor states and *p*-type property [32,33]. The charge density difference of the model was investigated to study the carrier transport process in the ZIS with S vacancies and P incorporation (Fig. 1d, e). The Zn, In, S, and P atoms are denoted by blue, purple, yellow, and red balls, respectively. These data indicate that an electron losing layer emerges near the S vacancies, while an electron accumulation layer appears close to the P atoms. As a result, the apparent difference of charge density would create a built-in electric field directing from top to bottom. Furthermore, the findings corroborate that S vacancies are associated with the *n*-type property, whereas P incorporation can introduce *p*-type property, in accordance with the above PDOS results. Specifically, from Fig. 1d, it could clearly be seen that the S vacancies mainly delivered the positive charges of the two atomic layers (Zn, S) in the top, while the P dopants rendered the two atomic layers (S, In) in the bottom negatively charged. Additionally, a transition region of electron transfer can be assigned to the middle atomic layers. According to these results, the *n*-type regions can be assigned to the two layers of atoms in the top, the *p*-type areas can be assigned to the two atomic layers in the bottom, whereas the *p*-*n* junctions can be assigned to the transition region of small charge changes (Fig. 1f). Accordingly, the DFT calculation results demonstrate the theoretical feasibility of building *p*-*n* junctions in single-unit-cell nanosheets. Moreover, the planar-averaged charge density difference for ZIS with S vacancies and ZIS with P incorporation were depicted in Fig. S1. We compared these data with the results of Fig. 1e to uncover the effects of such peculiar nanostructure on the separation of carriers. Fig. 1e clearly displayed that the changes of charge for every atomic layer were more obvious than those of the models in Fig. S1. Specifically, the bottom peaks of charge density difference (the blue shading) were evidently stronger than those of ZIS with S vacancies from Fig. S1b, whereas the top peaks (the yellow shading) were stronger than those of ZIS with P incorporation shown in Fig. S1d. It is well known that the bigger the charge difference between positively and negatively charged layers is, the stronger intensity of the built-in electric field will be. Collectively, these findings substantiate the better rectification effect of such unique *p*-*n* junctions originated from the stronger built-in electric field, which will enhance the overall efficiency of carrier separation/transfer.

3.2. Synthesis and characterizations

As shown in Fig. 2a, via a facile hydrothermal method, the atomically thin *n*-ZIS sheet arrays were fabricated on the FTO substrates. According to the data of ICP-OES (Table S2), it was notable that the proportion for S atoms of *n*-ZIS was significantly lower than that of perfect ZIS, manifesting the existence of a few S vacancies of *n*-ZIS, in agreement with the analysis of M−S plot in Fig. S2. Then the *n*-ZIS were processed by heat treatment in PH_3/Ar with various PH_3/(PH_3 + Ar) flow rate ratios (for more details, see Experimental). It should be noted that both the top and the bottom surfaces of nanosheet arrays were exposed to the reaction atmosphere during the phosphorization process. The corresponding products were respectively expressed as *n*-ZIS-P1, *n*-ZIS-P2, *n*-ZIS-P3, *n*-ZIS-P4, and *n*-ZIS-P5, based on the atomic ratios of 1%, 2%, 3%, 4%, and 5% for P/(Zn + In + S + P) from ICP-OES analysis. As revealed by SEM results in Fig. 2b, S3a, the vertically aligned sheet arrays were uniformly grown onto conductive substrates and the height of nanosheets was about 1.2 μm. Moreover, we also performed studies of how various reaction conditions impact the morphological feature of the products (Fig. S3-5).

The XRD analysis for the products manifested the characteristic peaks indexed to the hexagonal phase of ZIS, whereas no phase impurities were detected. (Fig. S6a). Compared with *n*-ZIS, the Raman peaks from *n*-ZIS-P2 and *n*-ZIS-P5 had a slight redshift (Fig. S6b), suggesting that P is doped into the *n*-ZIS lattice. A HRTEM image for *n*-ZIS-P2 from Fig. 2c revealed that the interplanar distances of 0.334 nm corresponds to the (100) lattice planes in hexagonal ZIS, showing inappreciable structural changes relative to *n*-ZIS (Fig. S7a). Furthermore, the corresponding fast Fourier transform (FFT) presented an ordered array of spots recorded from the [001] orientation (inset of Fig. 2d). Accordingly, the evidence confirmed that the arrangement of atoms in the crystal lattice of *n*-ZIS-P2 was relatively ordered, while there was the distorted crystal phase in the *n*-ZIS-P5 structure (Fig. S7b). The TEM image in Fig. S8 presented the nearly transparent feature of the sheet-like *n*-ZIS-P2. Moreover, the seven atomic layers of a nanosheet were clearly exhibited by HRTEM investigation of the cross-section and the thickness was approximately 1.24 nm (inset of Fig. S8). In Fig. 2e, the AFM images further demonstrated that the average thickness of ultrathin *n*-ZIS-P2 nanosheets was about 1.24 nm, in line with the 12.34 Å thickness of single-unit-cell ZIS along [001] axis (Fig. S9). The HAADF-STEM elemental mappings from the cross-sectional *n*-ZIS-P2 displayed that P was enriched on the In facet, whereas the distribution of the Zn, In, and S was

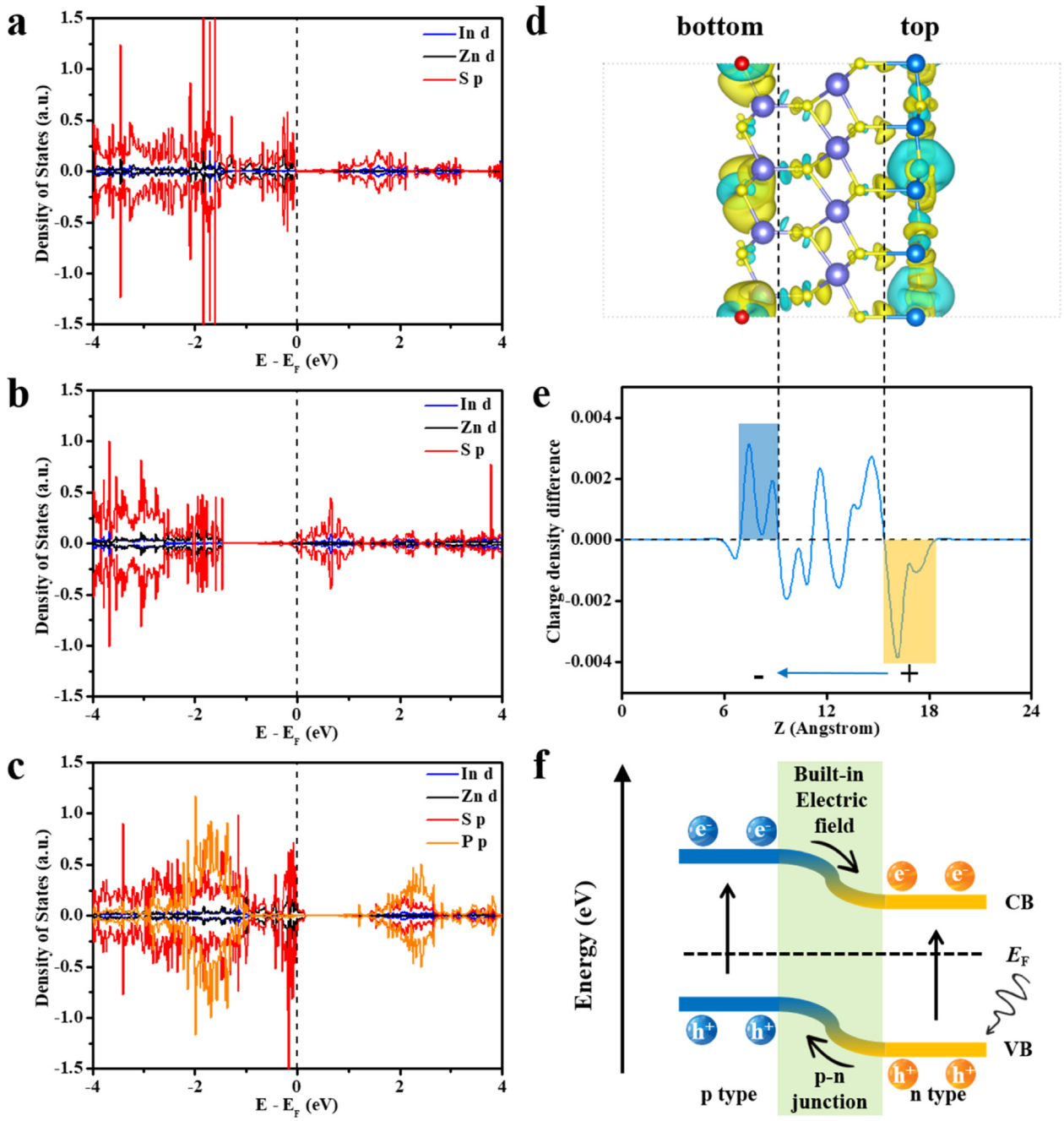

Fig. 1. The PDOS for a-c) pure ZIS, ZIS with S vacancies in the top layer, and ZIS with P incorporation in the bottom layer. d) The differential charge density map, e) the average difference electron density, and f) illustration for carrier transport of ZIS with S vacancies in the top layer and P incorporation in the bottom layer. The yellow and blue domains denote electron gaining and losing. (For interpretation of the references to colour in this figure legend, the reader is referred to the web version of this article.)

in conformity to the atomic arrangement in ZIS (Fig. 2f). Determined by the ICP-OES and EDS analyses of *n*-ZIS-P2 (Fig. S10), the atomic ratio of Zn, In, S, and P was about 1:2.01:3.68:0.15. As displayed in Fig. 2g, P 2p XPS spectra of *n*-ZIS-P2 showed that the peaks at 129.9 eV and 130.5 eV could be identified to P $2p_{3/2}$ and P $2p_{1/2}$, respectively, which could be identified as the P-Zn or P-In bonds [34,35]. Given that the binding energies for Zn 2p showed no significant change, the possibility of P-Zn bonding could be ruled out (Fig. S11a). Due to the surface exposed to air, there would be the peaks at 133.9 eV attributed to the slightly oxidization of P (P-O) [36,37]. Besides, the doped P had an inappreciable influence on the cation content (Fig. S11a, b), which was in line with the results of ICP-OES. With increasing the concentration of doping, the peak intensity for P 2p was enhanced, contrary to the results of S 2p peak (Fig. S11c). Collectively, the above analyses can reasonably infer that the P-In bonds are created through the substitution of P on S sites, consistent with the elemental mapping data.

3.3. Band structure analyses

UV–vis DRS indicated that the absorption edge of *n*-ZIS-P redshifted to a longer wavelength with respect to that of *n*-ZIS (Fig. S12). As the Tauc plots shown in the inset of Fig. S12a, the energy bandgap (E_g) for *n*-ZIS-P2 was reduced slightly compared with that for *n*-ZIS, indicating that the proper incorporation quantity of P has little influence on the capability of visible-light harvesting. As displayed in Fig. 3a, the positive and negative slopes

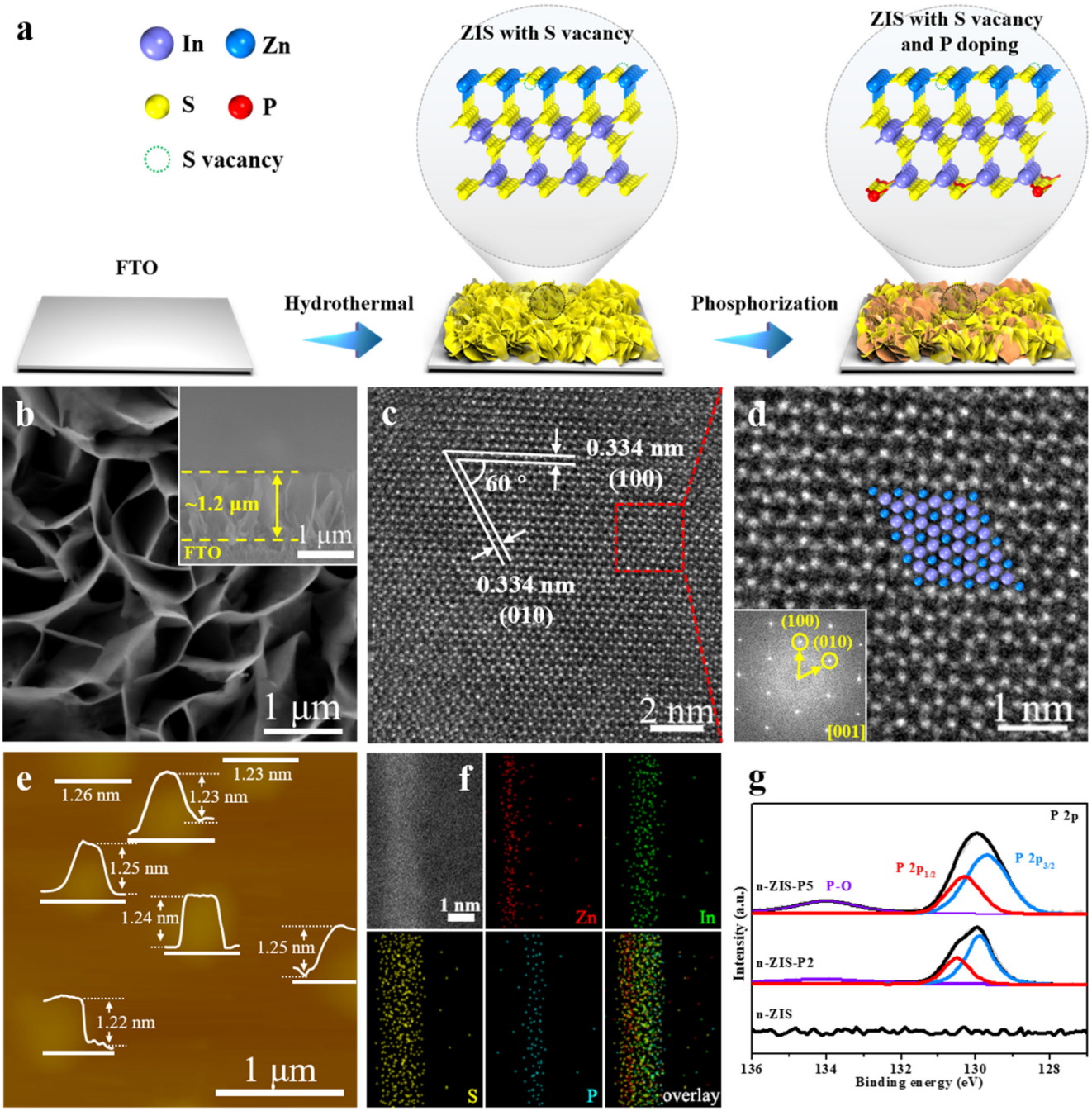

Fig. 2. a) The preparation process, b) SEM images and the inset is the cross-sectional view, c, d) HRTEM images and the inset of d is the homologous FFT pattern, e) AFM images with the corresponding height profiles confirmed along the lines presented in the insets, and f) HAADF-STEM image and the corresponding EDS elemental mapping of *n*-ZIS-P2. g) P 2p XPS comparison of *n*-ZIS, *n*-ZIS-P2, and *n*-ZIS-P5.

were found from diverse potential regions in the M–S plot of *n*-ZIS-P2, suggesting the coexistence of *n*- and *p*-type characteristics of the sample [38,39]. The phenomenon reveals that *n*- and *p*-type regions are respectively created by the S vacancies and the incorporated P, leading to the formation of *p*-*n* junctions in *n*-ZIS-P2. The extrapolation of the abscissa intercepts in M–S plot determined the E_F in *n*-ZIS-P2, and the E_F for *n*- and *p*-type feature areas are respectively represented as the symbols E_{Fn} and E_{Fp}. Besides, the changes of E_{Fn} and E_{Fp} in *n*-ZIS-P2 for 48 h were slight, indicating the good stability of the single-unit-cell *p*-*n* junction structure (Fig. S13a). Of note, considering that the E_{Fn} of *n*-ZIS and *n*-ZIS-P2 are similar (Fig. 3a, Fig. S2), to a certain extent, the E_{Fn} in *n*-ZIS-P2 is able to be represented by that in *n*-ZIS [40,41]. Additionally, as shown in Fig. S13b, the VBM value for *n*-ZIS-P2 was determined to be 1.30 eV versus RHE through linear potential anodic scans [40,42]. Accordingly, the value of CBM (-1.04 eV versus RHE) could be determined via the following formula, $E_{VBM} = E_g + E_{CBM}$.

UPS analyses were performed to further determine the band positions of *n*-ZIS-P2 (Fig. S13c, d). The secondary electron cutoff (E_{cutoff}) for *n*-ZIS and *n*-ZIS-P2 was respectively determined to be 17.6 eV and 16.8 eV. During the testing process, via the connections of the products with gold, the values for E_F were tuned to be 0 eV. Hence, work function (WF) of 3.62 eV versus vacuum in *n*-ZIS could be determined using the formula of $WF = h\nu + E_F - E_{cutoff}$ ($h\nu$ of 21.22 eV refers to the excitation energy of the He I Source Gun). The vacuum energy (E_{Vac}) determined by the results of UPS

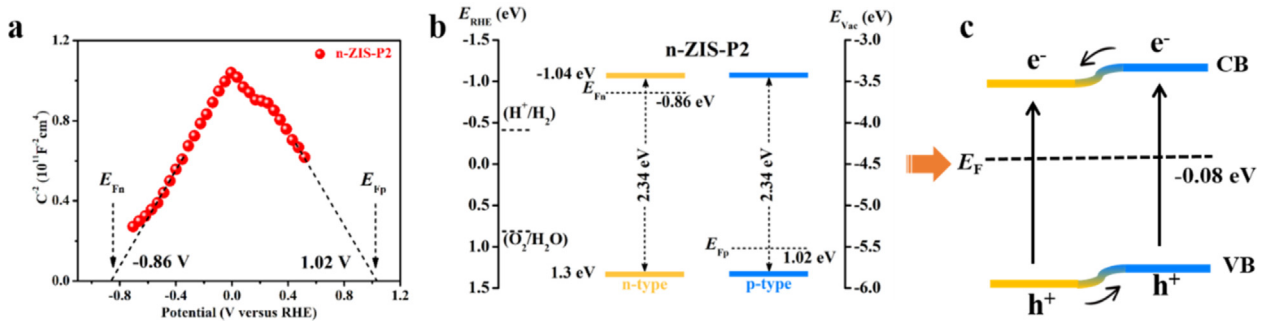

Fig. 3. a) M–S plot, b) the band structure alignment containing *n*- and *p*-type regions, and c) diagram for carrier transport of *n*-ZIS-P2.

could be transformed into the RHE potential (E_{RHE}) according to the formula $-E_{Vac} = E_{RHE} + 4.5$ eV [43]. Therefore, the VBM for *n*-ZIS-P2 could be determined to be 1.29 eV versus RHE, while the E_{Fn} for *n*-ZIS could be decided to be −0.88 eV versus RHE. Evidently, these data obtained from UPS were similar to those recorded from electrochemical tests for *n*-ZIS-P2, corroborating the reliability of the aforementioned data. Furthermore, the E_F for *n*-ZIS-P2 was situated at −0.08 eV versus RHE. In the light of the above results, Fig. 3b showed the band structure for *n*-ZIS-P2 containing both *n*- and *p*-type properties. Subsequently, the E_F alignment and *p*-*n* junctions would be formed by the coexistence of *n*- and *p*-type regions, thus creating strong built-in electric fields to promote carrier transport. (Fig. 3c). Overall, the observations convincingly demonstrate that the *p*-*n* junctions can be built in single-unit-cell sheet-like materials.

3.4. PEC properties for water splitting

The PEC water splitting tests of the samples were undertaken in 0.5 M Na_2SO_4 aqueous solution upon 1 sun radiation using an AM 1.5G solar simulator. As displayed in Fig. 4a, the *n*-ZIS-P2 photoanode delivered attractive activity and robust photostability for the PEC reaction of water splitting, presenting an admirable O_2 evolution amount of 308.9 μmol cm^{-2} at 1.23 V_{RHE}. Meanwhile, the produced H_2 on Pt electrode was 625.6 μmol cm^{-2}, revealing that the O_2 and H_2 were produced in the stoichiometric ratio (1:2). The Faradaic efficiency of O_2 and H_2 evolutions were 95% and 97%, respectively, reflecting that most photoexcited carriers are utilized for water splitting. Additionally, as shown in Fig. S14, the connection between P content and PEC water splitting performance presented a volcano-type trend, suggesting that the optimal atomic ratio of P/(Zn + In + S + P) is about 2%. Besides, the excellent stability was verified via various characterizations (XRD, SEM, TEM, and HRTEM) and M–S plot of the sample after reaction (Fig. S15). These results emphasize that the suitable introduction of acceptor dopants in single-unit-cell *n*-type photocatalysts can improve the PEC properties, benefited by the special structure of *p*-*n* junctions (Fig. 4b). It is also worth noting that the separated electrons can transfer fast to the substrates due to the *n*-type domain as an efficient electron conduction layer, instead of participating in the reduction reaction, as shown in Fig. 4b.

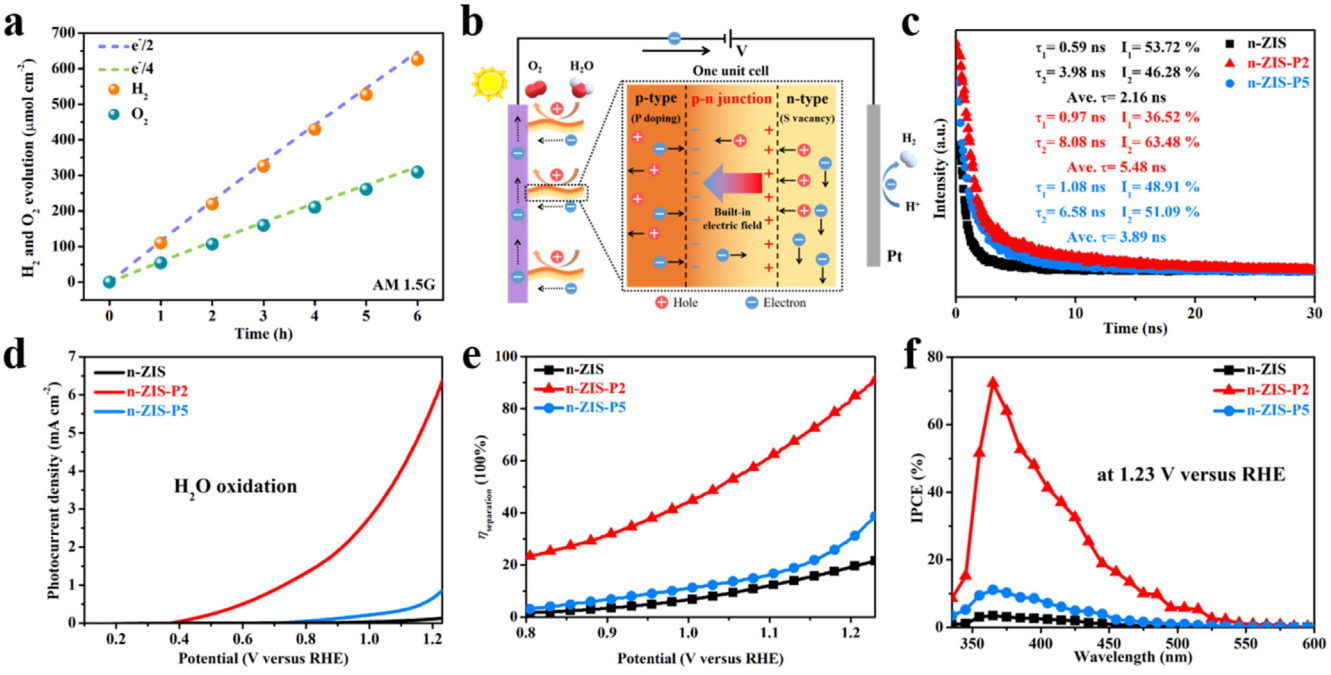

Fig. 4. a) Water splitting performance of *n*-ZIS-P2 photoanode tested at 1.23 V_{RHE}. The dash lines represent the theoretical amount of H_2 and O_2 calculated from photocurrent. b) Diagram of the structure of single-unit-cell *p*-*n* junctions in *n*-ZIS-P2. c) TRPL plots, d) the *J*-*V* curves in Na_2SO_4 (0.5 M) aqueous solution, e) the efficiency of charge separation, and f) IPCE curves of *n*-ZIS, *n*-ZIS-P2, and *n*-ZIS-P5 photoanodes.

3.5. The separation and transport of charge carriers

Various spectroscopy measurements were undertaken to obtain insights into the superior properties for *n*-ZIS-P2. In order to unveil the separation properties of photoinduced charge carriers, PL spectra were conducted (Fig. S16a). Obviously, the PL quenching of *n*-ZIS-P2 as compared to *n*-ZIS means the forcefully suppressed recombination of electron-hole pairs of *n*-ZIS-P2. Furthermore, SPV spectra showed a stronger SPV signal of *n*-ZIS-P2 than that of *n*-ZIS (Fig. S16b), owing to accelerated charge separation in *n*-ZIS-P2. For investigating charge dynamics in the products, TRPL measurement was considered a useful tool. As displayed in Fig. 4c, the *n*-ZIS-P2 presented longer lifetimes of charge carriers with respect to that of *n*-ZIS, due to more efficient charge transfer of *n*-ZIS-P2 [44]. Based on these observations, it is undoubted that the charge separation/transport efficiency can be promoted by constructing *p*-*n* junctions into single-unit-cell nanosheets, contributing to improving PEC performance. However, the *n*-ZIS-P5 sample presented unsatisfactory properties, implying that lattice distortion will induce too many electron-hole recombination centers, thereby decreasing their beneficial performance [45].

The photodeposition experiments were carried out to probe the carrier separation/migration behavior in the products. During the experiments, the photoreduced sediments were utilized to spot the positions of the photoinduced electrons, while the photooxidized sediments would occur in the places where the photoinduced holes reside. [46,47]. The SEM images for the *n*-ZIS-P2 sample exhibited that photodeposited Pt and Ag solely emerged on one side of the nanosheets, whereas such nanoparticles were difficult to find on the opposite side (Fig. S17a, b). Analogously, the photooxidized MnO_x and CoO_x were only deposited on one surface of the nanosheets (Fig. S17c, d). However, *n*-ZIS could merely result in small quantities of metal photodeposition as a result of severe recombination of light-excited charges and *n*-type property (Fig. S17e, f). To shed more light on the single-unit-cell *p*-*n* junctions structure, elemental mapping analyses were undertaken (Fig. S18). Pt tended to be located next to the Zn site while the deposition of MnO_x preferred to be formed near the P-incorporated site, manifesting the selective distribution of photoinduced charge carriers on the corresponding surface. To identify the reaction sites with both metal and metal oxides, the photodeposition experiments with both the two precursors of Pt and MnO_x in the solution were undertaken. The HAADF-STEM image and the corresponding elemental mapping images were clearly shown in Fig. S19. The Pt and MnO_x could be simultaneously photodeposited on the surfaces of the *n*-ZIS-P2 nanosheets. Specifically, the Pt sediments agglomerated on the surface of the Zn site, while the MnO_x were found on the surface around the P site. These findings further verify the creation of single-unit-cell *p*-*n* junctions structure and the direction for the built-in electric field constructed by this structure, in conformity to the results of DFT. XPS analyses were used to determine element valence states for the photodeposited products (Fig. S20). The XPS data disclose that the obtained Pt and Ag elements are at the states of metal, while the cobalt and manganese species are in the form of oxidation. These results uncover the promotional effects of the unique single-unit-cell *p*-*n* junctions on carrier separation/transportation.

3.6. Electrochemical characteristics

Multiple electrochemical characterizations were conducted to elucidate the improved PEC water-splitting properties of *n*-ZIS-P2. As shown in Fig. 4d, the *J*-*V* curves from water oxidation presented that the highest *J* of 6.34 mA cm^{-2} at 1.23 V_{RHE} was recorded, the circa 48-fold enhancement relative to *n*-ZIS, representing the increased photoactivity of *n*-ZIS-P2. The promotion of photoactivity was also proved by the *J*-*V* curves for sulfite oxidation (Fig. S21a). As far as we know, the highest *J* of water oxidation in n-ZIS-P2 is better than all the reported photoanodes based on ZIS (Table S3). As shown in Fig. S21b, the maximum HC-STH conversion efficiency of the *n*-ZIS-P2 photoanode was around 0.65% at 0.98 V_{RHE}, manifesting a significant improvement in efficiency compared with *n*-ZIS. In addition, based on the photocurrent from sulfite oxidation and water oxidation, Fig. 4e displayed the charge separation efficiency ($\eta_{separation}$) of the photoanodes, in which the $\eta_{separation}$ for *n*-ZIS-P2 was obviously higher than that for *n*-ZIS. The stability measurements showed that the *n*-ZIS-P2 photoanode can keep almost the same photocurrent density after 3600 s illumination, while the *n*-ZIS photoanode displayed obvious attenuation (Fig. S21c), suggesting the high PEC stability of *n*-ZIS-P2 photoanode. Moreover, electrochemical impedance spectra (EIS) tests were undertaken, and the obtained Nyquist plots indicated smaller semicircles of *n*-ZIS-P2 compared with those of *n*-ZIS (Fig. S21d, e), suggesting the improved interface carrier transfer for *n*-ZIS-P2. In addition, the IPCE plots depicted that *n*-ZIS-P2 had an evidently increased value of IPCE, and the highest value was approximately 72% at the wavelength of 365 nm (Fig. 4f), showing the promotion of separation/transfer efficiency of *n*-ZIS-P2. As for *n*-ZIS-P5, the substantial recombination of charge carriers is responsible for the low PEC activities, according to the spectroscopic analysis.

4. Conclusion

In conclusion, we propose a brand new *p*-*n* junction of single-unit-cell nanosheets and corroborate the theoretical and experimental feasibility of constructing such structure toward reinforced PEC properties. Giant improvement in PEC performance can be owing to the promoted charge separation/transport, suppressed recombination of electron–hole pairs, prolonged lifetime of charge carriers, and improved photostability. Our work would offer valuable insights into semiconductor physics research on the structure of *p*-*n* junctions and contribute to the developments of electronics and optoelectronics.

Author contributions

Yu Wang and Yu Wu developed the research concept. Yu Wu and Guangzhen Lv prepared the materials and performed the photoelectrochemical experiments. Shukai Yao, Yu Wu and Peilin Liao provided the theoretical calculations. Yu Wang, Peilin Liao, Yu Wu and Shukai Yao contributed to interpretation of the results and wrote the manuscript, which was revised by Yanwei Wang, Guangzhen Lv, and Huijuan Zhang. All authors contributed to the scientific discussions.

Declaration of Competing Interest

The authors declare that they have no known competing financial interests or personal relationships that could have appeared to influence the work reported in this paper.

Acknowledgements

This work was financially supported by the Fundamental Research Funds for the Central Universities (0301005202017, 2018CDQYFXCS0017, 106112017CDJXSYY0001), Thousand Young Talents Program of the Chinese Central Government (Grant No. 0220002102003), National Natural Science Foundation of China (NSFC, Grant No. U19A20100, 21971027, 21373280, 21403019), Beijing National Laboratory for Molecular Sciences (BNLMS) and

Hundred Talents Program at Chongqing University (Grant No. 0903005203205), The State Key Laboratory of Mechanical Transmissions Project (SKLMT-ZZKT-2017M11), Natural Science Foundation of Chongqing (Grant No. cstc2019jcyj-msxmX0426), Science and Technology Research Project of Education Agency in Chongqing (Grant No. KJZD-K201800102). P. L. acknowledges the donors of the American Chemical Society Petroleum Research Fund for partial support of this research. This research was supported in part through computational resources provided by the Information Technology department at Purdue, West Lafayette, Indiana.

Appendix A. Supplementary material

Supplementary data to this article can be found online at https://doi.org/10.1016/j.jcat.2021.08.009.

References

[1] K. Sivula, R.V. De Krol, Semiconducting materials for photoelectrochemical energy conversion, Nat. Rev. Mater. 1 (2016) 15010.
[2] N.S. Lewis, Research opportunities to advance solar energy utilization, Science 351 (2016) 353.
[3] S. Dahl, I. Chorkendorff, Solar-fuel generation: Towards practical implementation, Nat. Mater. 11 (2012) 100–101.
[4] M.G. Walter, E.L. Warren, J.R. Mckone, S.W. Boettcher, Q. Mi, E.A. Santori, N.S. Lewis, Solar water splitting cells, Chem. Rev. 110 (2010) 6446–6473.
[5] J. Hou, S. Cao, Y. Sun, Y. Wu, F. Liang, Z. Lin, L. Sun, Atomically thin mesoporous In_2O_{3-x}/In_2S_3 lateral heterostructures enabling robust broadband-light photoelectrochemical water splitting, Adv. Energy Mater. 8 (2018) 1701114.
[6] M. Zhou, X.W.(. Lou, Y.i. Xie, Two-dimensional nanosheets for photoelectrochemical water splitting: Possibilities and opportunities, Nano Today 8 (6) (2013) 598–618.
[7] M. Xiao, B. Luo, M. Lyu, S. Wang, L. Wang, Single-crystalline nanomesh tantalum nitride photocatalyst with improved hydrogen-evolving performance, Adv. Energy Mater. 8 (2018) 1701605.
[8] Q. Han, X. Bai, Z. Man, H. He, L. Li, J. Hu, A. Alsaedi, T. Hayat, Z. Yu, W. Zhang, Convincing synthesis of atomically thin, single-crystalline $InVO_4$ sheets toward promoting highly selective and efficient solar conversion of CO_2 into CO, J. Am. Chem. Soc. 141 (2019) 4209–4213.
[9] L. Meng, X. Zhou, S. Wang, Y. Zhou, W. Tian, P. Kidkhunthod, S. Tunmee, Y. Tang, R. Long, Y. Xin, A plasma-triggered O-S bond and P-N junction near the surface of a SnS_2 nanosheet array to enable efficient solar water oxidation, Angew. Chem., Int. Ed. 58 (2019) 16668–16675.
[10] Z. Liu, L. Wang, X. Yu, J. Zhang, R. Yang, X. Zhang, Y. Ji, M. Wu, L. Deng, L. Li, Piezoelectric-effect-enhanced full-spectrum photoelectrocatalysis in p–n heterojunction, Adv. Funct. Mater. 29 (2019) 1807279.
[11] H. Wang, L. Zhang, Z. Chen, J. Hu, S. Li, Z. Wang, J. Liu, X. Wang, Semiconductor heterojunction photocatalysts: design, construction, and photocatalytic performances, Chem. Soc. Rev. 43 (2014) 5234–5244.
[12] I. Yoo, S.S. Kalanur, H. Seo, A nanoscale p–n junction photoelectrode consisting of an NiO_x layer on a TiO_2/CdS nanorod core-shell structure for highly efficient solar water splitting, Appl. Catal., B 250 (2019) 200–212.
[13] J. Zhang, P. Li, H. Sun, X. Shen, T. Deng, K. Zhu, Q. Zhang, J. Wu, Ultraviolet electroluminescence from controlled arsenic-doped ZnO nanowire homojunctions, Appl. Phys. Lett. 93 (2008) 021116.
[14] A. Azcatl, X. Qin, A. Prakash, C. Zhang, L. Cheng, Q. Wang, N. Lu, M.J. Kim, J. Kim, K. Cho, Covalent nitrogen doping and compressive strain in MoS_2 by remote N_2 plasma exposure, Nano Lett. 16 (2016) 5437–5443.
[15] Z. Ai, Y. Shao, B. Chang, L. Zhang, J. Shen, Y. Wu, B. Huang, X. Hao, Rational modulation of p-n homojunction in P-doped g-C_3N_4 decorated with Ti_3C_2 for photocatalytic overall water splitting, Appl. Catal., B 259 (2019) 118077.
[16] C.-H. Lee, G.-H. Lee, A.M. van der Zande, W. Chen, Y. Li, M. Han, X.u. Cui, G. Arefe, C. Nuckolls, T.F. Heinz, J. Guo, J. Hone, P. Kim, Atomically thin p–n junctions with van der Waals heterointerfaces, Nat. Nanotechnol. 9 (9) (2014) 676–681.
[17] T.W. Kim, K.-S. Choi, Nanoporous $BiVO_4$ photoanodes with dual-layer oxygen evolution catalysts for solar water splitting, Science 343 (6174) (2014) 990–994.
[18] Y.-S. Chen, J.S. Manser, P.V. Kamat, All solution-processed lead halide perovskite-$BiVO_4$ tandem assembly for photolytic solar fuels production, J. Am. Chem. Soc. 137 (2) (2015) 974–981.
[19] D.A. Reddy, K.A.J. Reddy, D.H. Hong, M. Gopannagari, D.P. Kumar, T.K. Kim, Constructing ordered paths to improve the charge separation and light harvesting capacity towards efficient solar water oxidation performance, Appl. Catal., B 269 (2020) 118761, https://doi.org/10.1016/j.apcatb.2020.118761.
[20] G. Kresse, J. Furthmüller, Efficient iterative schemes for ab initio total-energy calculations using a plane-wave basis set, Phys. Rev. B 54 (16) (1996) 11169–11186.
[21] G. Kresse, J. Furthmüller, Efficiency of ab-initio total energy calculations for metals and semiconductors using a plane-wave basis set, Comput. Mater. Sci. 6 (1) (1996) 15–50.
[22] P.E. Blöchl, Projector augmented-wave method, Phys. Rev. B 50 (24) (1994) 17953–17979.
[23] J.P. Perdew, K. Burke, M. Ernzerhof, Generalized gradient approximation made simple, Phys. Rev. Lett. 77 (18) (1996) 3865–3868.
[24] A.I. Liechtenstein, V.I. Anisimov, J. Zaanen, Density-functional theory and strong-interactions-orbital ordering in mott-hubbard insulators, Phys. Rev. B 52 (8) (1995) R5467–R5470.
[25] S.L. Dudarev, G.A. Botton, S.Y. Savrasov, C.J. Humphreys, A.P. Sutton, Electron-energy-loss spectra and the structural stability of nickel oxide : An LSDA+U study, Phys. Rev. B 57 (1998) 1505–1509.
[26] K. Yu, E.A. Carter, Communication: comparing ab initio methods of obtaining effective U parameters for closed-shell materials, J. Chem. Phys. 140 (12) (2014) 121105, https://doi.org/10.1063/1.4869718.
[27] K. Yu, E.A. Carter, A strategy to stabilize kesterite CZTS for high-performance solar cells, Chem. Mater. 27 (8) (2015) 2920–2927.
[28] S.I. Radautsan, F.G. Donika, G.A. Kyosse, I.G. Mustya, Polytypism of ternary phases in the system ZnInS, Phys. Status Solidi 37 (2) (1970) K123–K127.
[29] Y.J. Zhang, H.M. Tang, S.-P. Gao, Density functional theory study of $ZnIn_2S_4$ and $CdIn_2S_4$ polymorphs using full-potential linearized augmented plane wave method and modified Becke-Johnson Potential, Phys. Status Solidi B 257 (1) (2020) 1900485, https://doi.org/10.1002/pssb:v257.110.1002/pssb:201900485.
[30] R. Zhang, Y. Fang, T. Chen, F. Qu, Z. Liu, G.u. Du, A.M. Asiri, T. Gao, X. Sun, Enhanced photoelectrochemical water oxidation performance of Fe_2O_3 nanorods array by S doping, ACS Sustain. Chem. Eng. 5 (9) (2017) 7502–7506.
[31] Y. Liu, Y. Cai, G. Zhang, Y.-W. Zhang, K.-W. Ang, Al-doped black phosphorus p–n homojunction diode for high performance photovoltaic, Adv. Funct. Mater. 27 (7) (2017) 1604638, https://doi.org/10.1002/adfm.v27.710.1002/adfm.201604638.
[32] J.-K. Qin, W.-Z. Shao, C.-Y. Xu, Y. Li, D.-D. Ren, X.-G. Song, L. Zhen, Chemical vapor deposition growth of degenerate p-Type Mo-Doped ReS_2 films and their homojunction, ACS Appl. Mater. Interfaces 9 (18) (2017) 15583–15591.
[33] C. Lv, G. Chen, X. Zhou, C. Zhang, Z. Wang, B. Zhao, D. Li, Oxygen-induced Bi^{5+}-self-doped $Bi_4V_2O_{11}$ with a p–n homojunction toward promoting the photocatalytic performance, ACS Appl. Mater. Interfaces 9 (28) (2017) 23748–23755.
[34] S. Kouser, S.R. Lingampalli, P. Chithaiah, A. Roy, S. Saha, U.V. Waghmare, C.N.R. Rao, Extraordinary changes in the electronic structure and properties of CdS and ZnS by anionic substitution: cosubstitution of P and Cl in Place of S†, Angew. Chem., Int. Ed. 54 (28) (2015) 8149–8153.
[35] H. Virieux, M. Le Troedec, A. Cros-Gagneux, W.-S. Ojo, F. Delpech, C. Nayral, H. Martinez, B. Chaudret, InP/ZnS nanocrystals: Coupling NMR and XPS for fine surface and interface description, J. Am. Chem. Soc. 134 (48) (2012) 19701–19708.
[36] J. Yang, F. Zhang, X. Wang, D. He, G. Wu, Q. Yang, X. Hong, Y. Wu, Y. Li, Porous molybdenum phosphide nano-octahedrons derived from confined phosphorization in UIO-66 for efficient hydrogen evolution, Angew. Chem., Int. Ed. 55 (2016) 12854–12858.
[37] M. Yi, B. Lu, X. Zhang, Y. Tan, Z. Zhu, Z. Pan, J. Zhang, Ionic liquid-assisted synthesis of nickel cobalt phosphide embedded in N, P codoped-carbon with hollow and folded structures for efficient hydrogen evolution reaction and supercapacitor, Appl. Catal., B 283 (2021) 119635.
[38] G. Liu, G. Zhao, W. Zhou, Y. Liu, H. Pang, H. Zhang, D. Hao, X. Meng, P. Li, T. Kako, In Situ bond modulation of graphitic carbon nitride to construct p–n homojunctions for enhanced photocatalytic hydrogen production, Adv. Funct. Mater. 26 (2016) 6822–6829.
[39] T. Wang, Y. Wei, X. Chang, C. Li, A. Li, S. Liu, J. Zhang, J. Gong, Homogeneous Cu_2O p-n junction photocathodes for solar water splitting, Appl. Catal., B 226 (2018) 31–37.
[40] T.F. Yeh, C.Y. Teng, S. Chen, H. Teng, Nitrogen-doped graphene oxide quantum dots as photocatalysts for overall water-splitting under visible light illumination, Adv. Mater. 26 (2014) 3297–3303.
[41] Y.-C. Wang, C.-Y. Chang, T.-F. Yeh, Y.-L. Lee, H. Teng, Formation of internal p–n junctions in Ta_3N_5 photoanodes for water splitting, J. Mater. Chem. A 2 (48) (2014) 20570–20577.
[42] S. Hu, W. Yang, N. Li, H. Wang, J. Yang, Q. Chang, Carbon-dot-based heterojunction for engineering band-edge position and photocatalytic performance, Small 14 (44) (2018) 1803447, https://doi.org/10.1002/smll.v14.4410.1002/smll.201803447.
[43] A. Paracchino, N. Mathews, T. Hisatomi, M. Stefik, S.D. Tilley, M. Grätzel, Ultrathin films on copper(I) oxide water splitting photocathodes: a study on performance and stability, Energy Environ. Sci. 5 (9) (2012) 8673, https://doi.org/10.1039/c2ee22063f.
[44] D. Zhao, Y. Yu, C. Wang, W. Liao, N. Shrestha, C.R. Grice, A.J. Cimaroli, L. Guan, R. J. Ellingson, K. Zhu, X. Zhao, R.-G. Xiong, Y. Yan, Low-bandgap mixed tin–lead iodide perovskite absorbers with long carrier lifetimes for all-perovskite tandem solar cells, Nat. Energy 2 (4) (2017), https://doi.org/10.1038/nenergy.2017.18.
[45] P. Wang, Z. Shen, Y. Xia, H. Wang, L. Zheng, W. Xi, S. Zhan, Atomic insights for optimum and excess doping in photocatalysis: A case study of few-layer Cu-$ZnIn_2S_4$, Adv. Funct. Mater. 29 (3) (2019) 1807013, https://doi.org/10.1002/adfm.v29.310.1002/adfm.201807013.

[46] J. Li, L. Cai, J. Shang, Y. Yu, L. Zhang, Giant enhancement of internal electric field boosting bulk charge separation for photocatalysis, Adv. Mater. 28 (2016) 4059–4064.

[47] Z. Li, L. Zhang, Y. Liu, C. Shao, Y. Gao, F. Fan, J. Wang, J. Li, J. Yan, R. Li, Surface-polarity-induced spatial charge separation boosts photocatalytic overall water splitting on GaN nanorod arrays, Angew. Chem., Int. Ed. 59 (2020) 935–942.